

Effective potentials in a rotating spin-orbit-coupled spin-1 spinor condensate

Paramjeet Banger^{1*}, R. Kishor Kumar^{2†}, Arko Roy^{3‡}, and Sandeep Gautam^{1§}

¹*Department of Physics, Indian Institute of Technology Ropar, Rupnagar 140001, Punjab, India*

²*Department of Physics, Centre for Quantum Science, and Dodd-Walls Centre for Photonic and Quantum Technologies, University of Otago, Dunedin 9054, New Zealand and*

³*School of Physical Sciences, Indian Institute of Technology Mandi, Mandi-175075 (H.P.), India*

We theoretically study the stationary-state vortex lattice configurations of rotating spin-orbit- and coherently-coupled spin-1 Bose-Einstein condensates trapped in quasi-two-dimensional harmonic potentials. The combined effects of rotation, spin-orbit and coherent couplings are analyzed systematically from the single-particle perspective. Through the single-particle Hamiltonian, which is exactly solvable for one-dimensional coupling, under specific coupling and rotation strengths, we illustrate that a boson in these rotating spin-orbit- and coherently-coupled condensates are subjected to effective toroidal, symmetric double-well, or asymmetric double-well potentials. In the presence of mean-field interactions, using the coupled Gross-Pitaevskii formalism at moderate to high rotation frequencies, the analytically obtained effective potential minima and the numerically obtained coarse-grained density maxima position are in excellent agreement. On rapid rotation, we further find that the spin-expectation per particle of an antiferromagnetic spin-1 Bose-Einstein condensate approaches unity indicating a similarity in the response with ferromagnetic spin-orbit-coupled condensates.

PACS numbers:

I. INTRODUCTION

The experimental realization of artificial gauge fields [1, 2] and spin-orbit (SO) coupling between the spin and the linear momentum of electrically neutral bosons [3] opened a hitherto inaccessible research direction to the researchers. An SO coupling, which couples the three magnetic sublevels of spin-1 ⁸⁷Rb, wherein Rashba [4] and Dresselhaus [5] couplings contribute with equal weights has been realized in an experiment [6]. More recently, using an optical Raman lattice, two-dimensional SO coupling and the resulting topological bands have been experimentally realised with ⁸⁷Rb involving two of its hyperfine spin states [7]. In spin-1 Bose-Einstein condensates (BECs), SO coupling results in diverse ground-state phases like plane-wave, stripe or standing-wave, vortex-lattice, zero-momentum phases, etc. [8–11]. Besides these unusual phases, self-trapped vortex solitons [12, 13], knotted solitons [14], super-stripes, and super-lattices [15] can also emerge as the ground state solutions of the SO-coupled spin-1 BECs in different parameter domains. Furthermore, coupling between the spin and orbital angular momentum of a neutral bosonic atom has also been experimentally realized recently [16, 17].

The realization of the SO coupling has made it possible to explore the interplay of synthetic non-Abelian and Abelian gauge potential arising due to rotation [18], e.g. in the two-component SO- [19–24] or coherently-coupled pseudospin-1/2 BECs [25]. In spin-1 BECs, the inter-

action between Rashba SO coupling and rotation under rapid quenching leading to half-skyrmion excitations [26], hexagonal lattice of skyrmions and a square lattice of half-quantized vortices [27] has already been theoretically investigated. It has also been shown numerically that a rotating spin-1 BEC with anisotropic SO coupling can support vortex-chain solutions [28, 29], whereas the presence of an isotropic Rashba SO coupling may result in a vortex lattice with a hexagonal or an approximate square lattice pattern [30]. The numerical studies on ground states of rotating Rashba SO-coupled gases in concentrically coupled toroidal traps [31], rotating ferromagnetic BEC with isotropic three-dimensional SO coupling [32], and SU(3) coupling subjected to a magnetic-field gradient [33] are among the other investigations which deserve to be mentioned. More recently, topological vortical phase transitions in an SO-coupled spin-2 BEC under rotation have been theoretically studied [34].

In this paper, we highlight the combined effects of spin-exchange interactions, SO and coherent couplings, and rotation frequency on spin-1 condensates. We consider a quasi-two-dimensional harmonically trapped spinor condensate with a generic Rashba SO coupling of the form $\propto (\gamma_x S_x \partial/\partial x + \gamma_y S_y \partial/\partial y)$ [4] and a coherent coupling. Here S_x and S_y are the spin operators for the spin-1 system and γ_x and γ_y are the SO-coupling strengths. We proceed to study the stationary-state solutions with a focus primarily on moderate to large rotation frequencies of up to 0.95 times of the trapping frequency and within the domain of validity of the mean-field model. It is important to point out that the celebrated experimental realization of SO coupling [3] corresponds to one dimensional coupling $\gamma_x S_x p_x$ with a non-zero coherent coupling. To execute our studies, from a single-particle perspective, we examine in detail the effective potential arising out of rotation, SO, and coherent couplings and

*2018phz0003@iitrpr.ac.in

†kishor.ramavarmaraja@otago.ac.nz

‡arko@iitmandi.ac.in

§sandeep@iitrpr.ac.in

relate it to the scalar and vector potentials experienced by a boson for an experimentally relevant case. We compute the spin-expectation per particle as a function of rotation frequency and one of the key findings of the work is a similarity in the response of SO-coupled ^{87}Rb (ferromagnetic) and ^{23}Na (antiferromagnetic) BECs at moderate to large rotations; we also examine the spin-texture at small and large rotation frequencies to buttress this point. The inclusion of one-dimensional SO coupling, i.e., $\gamma_x \neq 0, \gamma_y = 0$, coherent coupling, and a theoretical analysis of an SO-coupled single-particle Hamiltonian leading to the evaluation of effective potentials makes this study distinct from earlier studies on SO-coupled BECs under rotation [20, 30].

The paper is organized as follows. The analytic solutions of the single-particle Hamiltonian corresponding to the SO- and coherently-coupled bosons under rotation are provided in Sec. II. To describe the realistic experimental scenario, the mean-field density and spin-dependent interaction terms are included to formulate the coupled Gross-Pitaevskii equations (GPEs) in Sec. III. The stationary-state solutions for the interacting SO- and coherently-coupled ^{87}Rb and ^{23}Na spin-1 BECs in a rotating frame are then obtained and discussed in Sec. III A. The response of the system is further explored through the computation of the spin-expectation per particle as a function of rotation frequency and illustrated in Sec. III B. We conclude highlighting the main results in Sec. IV.

II. SINGLE-PARTICLE PICTURE

Under a two-dimensional harmonic confinement, the Hamiltonian of an SO- and coherently-coupled spin-1 boson in the rotating frame in the dimensionless form is given by [20, 31]

$$H_0 = \left[\frac{p_x^2 + p_y^2}{2} + V(x, y) - \Omega_{\text{rot}} L_z \right] \mathbb{1} + \gamma_x S_x p_x + \gamma_y S_y p_y + \Omega_{\text{coh}} S_x, \quad (1)$$

where $p_\nu = -i\partial/\partial\nu$ with $\nu = (x, y)$, $V(x, y) = (x^2 + y^2)/2$ is an isotropic harmonic trapping potential, Ω_{rot} is the angular frequency of rotation around z axis, $L_z = (xp_y - yp_x)$ is the z component of the angular-momentum operator, $\mathbb{1}$ is a 3×3 identity matrix, γ_x and γ_y are the SO-coupling strengths, Ω_{coh} is the coherent-coupling strength, and S_ν is the irreducible representations of angular momentum operator for a spin-1 system. The units of length, time, energy, and energy eigenfunctions are considered to be $a_{\text{osc}} = \sqrt{\hbar/(m\omega_x)}$, ω_x^{-1} , $\hbar\omega_x$, and a_{osc}^{-1} , respectively, where m is the mass of the boson and ω_x is the harmonic oscillator frequency along x direction. To delineate the combined effect of rotation, SO, and coherent couplings, we calculate the minimum-energy eigenfunctions and eigenenergies of the Hamiltonian for two analytically tractable cases:

$$\gamma_x \neq 0, \gamma_y = 0, \Omega_{\text{coh}} \neq 0, \quad (2a)$$

$$\gamma_x = \gamma_y \neq 0, \Omega_{\text{coh}} = 0, \quad (2b)$$

where (2a) represents an experimentally realizable equal-strength mixture of Rashba and Dresselhaus couplings [3, 6], which couples the spin with the linear momentum along x direction, and the latter (2b) employs the Rashba SO coupling [4] which couples the spin with linear momentum along xy plane.

The calculation of the eigen-spectrum of H_0 in the former case (2a) is facilitated by a unitary transformation, $H_0 \rightarrow U^\dagger H_0 U$ with

$$U = \begin{pmatrix} 1/2 & -1/\sqrt{2} & 1/2 \\ 1/\sqrt{2} & 0 & -1/\sqrt{2} \\ 1/2 & 1/\sqrt{2} & 1/2 \end{pmatrix}, \quad (3)$$

as the rotation operator. The operator U rotates the spin state about y axis in an anticlockwise direction by an angle $\pi/2$ [35]. The transformed Hamiltonian $U^\dagger H_0 U = \text{diag}(h_{+1}, h_0, h_{-1})$, where $\text{diag}(\dots)$ stands for a 3×3 diagonal matrix (operator). The operators h_j s are

$$h_j = \frac{(p_x + \frac{j\gamma_x}{1-\Omega_{\text{rot}}^2} + \Omega_{\text{rot}}\bar{y})^2}{2} + \frac{(p_{\bar{y}} - \Omega_{\text{rot}}x)^2}{2} + (1 - \Omega_{\text{rot}}^2) \frac{(x^2 + \bar{y}^2)}{2} - \frac{j^2\gamma_x^2}{2(1 - \Omega_{\text{rot}}^2)} + j\Omega_{\text{coh}}, \quad (4)$$

where $j = 0, \pm 1$, $\bar{y} = y - j\gamma_x\Omega_{\text{rot}}/(1 - \Omega_{\text{rot}}^2)$ and $p_{\bar{y}} = -i\partial/\partial\bar{y}$ is the canonical conjugate momentum of \bar{y} . The decoupled eigenvalue equation for h_j is $h_j\psi_j(x, \bar{y}) = E_j\psi_j(x, \bar{y})$ which can be simplified by substituting $\psi_j(x, \bar{y}) = \bar{\psi}_j(x, \bar{y}) \exp\left(-i\frac{j\gamma_x}{1-\Omega_{\text{rot}}^2}x\right)$ to obtain

$$\left[\frac{p_x^2 + p_{\bar{y}}^2}{2} + \frac{x^2 + \bar{y}^2}{2} - \Omega_{\text{rot}}(xp_{\bar{y}} - \bar{y}p_x) - \frac{j^2\gamma_x^2}{2(1 - \Omega_{\text{rot}}^2)} + j\Omega_{\text{coh}} \right] \bar{\psi}_j(x, \bar{y}) = E_j \bar{\psi}_j(x, \bar{y}). \quad (5)$$

The Hamiltonian on the left hand side of Eq. (5), barring the constant terms, is that of a two-dimensional isotropic harmonic oscillator under rotation. It is to be noted that the eigenfunctions of this Hamiltonian are also the eigenfunctions of the Hamiltonian representing a isotropic harmonic oscillator in the absence of rotation which commutes with L_z [35]. The ground state eigenenergy is, therefore, given by

$$E_j = \frac{2(1 + j\Omega_{\text{coh}})(1 - \Omega_{\text{rot}}^2) - j^2\gamma_x^2}{2(1 - \Omega_{\text{rot}}^2)}, \quad (6)$$

and the corresponding eigenstate is $\bar{\psi}_j(x, \bar{y}) = \frac{1}{\sqrt{\pi}} \exp\left(-\frac{x^2 + \bar{y}^2}{2}\right)$. On the x - y plane, we thus obtain

$$\psi_j(x, y) = \frac{1}{\sqrt{\pi}} \exp \left[-\frac{x^2 + \left(y - \frac{j\gamma_x\Omega_{\text{rot}}}{1-\Omega_{\text{rot}}^2}\right)^2}{2} - i\frac{j\gamma_x}{1-\Omega_{\text{rot}}^2}x \right]. \quad (7)$$

The three minimum-energy vector eigenfunctions of the original Hamiltonian H_0 with eigenenergies E_j s can now simply be written as $\Phi_j(x, y) = \psi_j(x, y)U\zeta_j$, where U and $\psi_j(x, y)$ are defined in Eqs. (3) and (7), respectively. Here ζ_j s are the three eigenvectors of S_z : $\zeta_{+1} = (1, 0, 0)^T$, $\zeta_0 = (0, 1, 0)^T$, and $\zeta_{-1} = (0, 0, 1)^T$, where T denotes the transpose. In the absence of coherent coupling, $\Omega_{\text{coh}} = 0$, the eigenfunctions $\Phi_{-1}(x, y)$ and $\Phi_{+1}(x, y)$ become degenerate having the least energy. Under these considerations, the principle of linear superposition further admits $c_+\Phi_{+1} + c_-\Phi_{-1}$ to be a possible degenerate eigenfunction subject to the constraint $|c_+|^2 + |c_-|^2 = 1$. In the presence of infinitesimally small repulsive interactions, say spin-independent interactions, the interaction energy is minimized if $|c_+| = |c_-| = 1/\sqrt{2}$ resulting in a equal-strength mixture of $\Phi_{\pm 1}(x, y)$. The resultant density, $[|\psi_{+1}(x, y)|^2 + |\psi_{-1}(x, y)|^2]/2$, is bimodal with equal-height peaks at $(0, \pm\gamma_x\Omega_{\text{rot}}/(1-\Omega_{\text{rot}}^2))$; this is indeed reflective of an effective two-well potential experienced by the boson. The presence of coherent coupling $\Omega_{\text{coh}} \neq 0$, however, results in the lifting of the degeneracy between $\Phi_{-1}(x, y)$ and $\Phi_{+1}(x, y)$ with $\Delta E = E_{+1} - E_{-1} = 2\Omega_{\text{coh}}$.

The exact effective potential experienced by the boson can also be computed through vector and scalar potentials [19]. To identify these potentials for the former case (2a), we rewrite h_j in Eq. (4) as

$$h_j = \frac{(p_x - A_x^j)^2}{2} + \frac{(p_y - A_y^j)^2}{2} + W_j(x, y) + V(x, y), \quad (8)$$

where $A_x^j = -j\gamma_x - \Omega_{\text{rot}}y$, $A_y^j = \Omega_{\text{rot}}x$ are the x and y components of the vector potential, and the scalar potential $W_j(x, y) = [2j\Omega_{\text{coh}} - j^2\gamma^2 - 2j\gamma\Omega_{\text{rot}}y - \Omega_{\text{rot}}^2(x^2 + y^2)]/2$. With these definitions, the effective potentials [19] for $j = 0, \pm 1$ are given as

$$V_{\text{eff}}^j(x, y) = \frac{1}{2} [(1 - \Omega_{\text{rot}}^2)(x^2 + y^2) - j^2\gamma_x^2 + 2j\Omega_{\text{coh}} - 2j\gamma_x\Omega_{\text{rot}}y]. \quad (9)$$

From Eq. (9), $V_{\text{eff}}^{+1}(x, y)$ and $V_{\text{eff}}^{-1}(x, y)$ overlap at $y = \Omega_{\text{coh}}/\gamma_x\Omega_{\text{rot}}$ for $\gamma_x \neq 0$ and $\Omega_{\text{rot}} \neq 0$. In the region, $y < \Omega_{\text{coh}}/\gamma_x\Omega_{\text{rot}}$, V_{eff}^{-1} is lower than the other two and with a minima at $\gamma_x\Omega_{\text{rot}}/(1 - \Omega_{\text{rot}}^2)$, whereas for $y > \Omega_{\text{coh}}/\gamma_x\Omega_{\text{rot}}$, V_{eff}^{+1} is the low lying potential curve with a minima at $-\gamma_x\Omega_{\text{rot}}/(1 - \Omega_{\text{rot}}^2)$. Which are also the positions of the density maxima of $|\Phi_{\pm 1}(x, y)|^2$, as discussed earlier. We illustrate the effective potential energy curves for the two representative cases with $\gamma_x = 1$ and $\gamma_y = \Omega_{\text{coh}} = 0$: under a moderate rotation frequency ($\Omega_{\text{rot}} = 0.5$) in Fig. 1(a) and a high rotation frequency ($\Omega_{\text{rot}} = 0.95$) in Fig. 1(b). The potentials thus experienced by the boson are effectively equivalent to symmetric double-well potentials with minima occurring at $(x = 0, y \mp 0.67)$ and $(x = 0, y \mp 9.74)$, respectively. Depending on the values of γ_x and γ_y , the presence of the

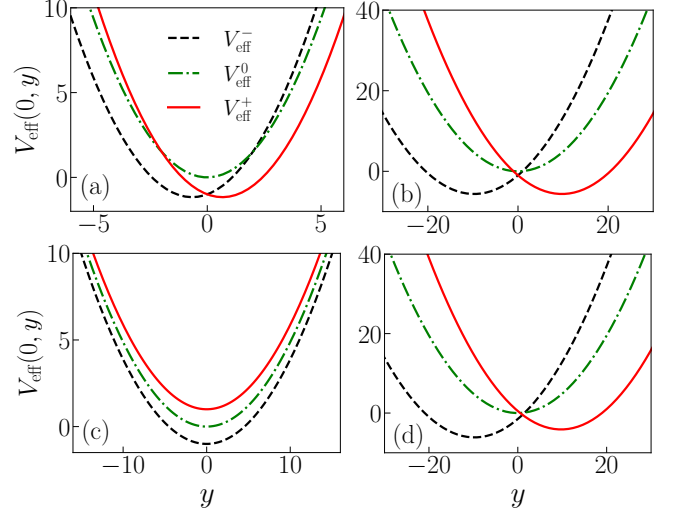


FIG. 1: (Color online) Sketch of the effective potential V_{eff}^j , viz. Eq. (9), along y -axis: (a) $\gamma_x = 1$, $\gamma_y = 0$, $\Omega_{\text{coh}} = 0$, and $\Omega_{\text{rot}} = 0.5$, (b) $\gamma_x = 1$, $\gamma_y = 0$, $\Omega_{\text{coh}} = 0$, and $\Omega_{\text{rot}} = 0.95$, (c) $\gamma_x = 0$, $\gamma_y = 0$, $\Omega_{\text{coh}} = 1$, and $\Omega_{\text{rot}} = 0.95$, and (d) $\gamma_x = 1$, $\gamma_y = 0$, $\Omega_{\text{coh}} = 1$, and $\Omega_{\text{rot}} = 0.95$.

coherent coupling modifies the effective potential landscape in different ways, for example, with $\Omega_{\text{coh}} = 1$ it is harmonic potential for $\gamma_x = \gamma_y = 0$ with minima at origin and an asymmetric double-well potential for $\gamma_x = 1$ and $\gamma_y = 0$ with a global minima at $(x = 0, y = -9.74)$. These are, respectively, shown in Figs. 1(c) and (d).

For the latter case (2b), namely $\gamma_x = \gamma_y = \gamma$ and $\Omega_{\text{coh}} = 0$, the eigenvalue problem for the Hamiltonian H_0 is not exactly solvable. We, therefore, use the variational method to calculate an approximate minimum-energy solution considering the following variational *ansatz* in polar coordinates

$$\Phi_{\text{var}}(r, \phi) = \frac{\exp\left(-\frac{r^2}{2\sigma^2}\right)}{\sqrt{\pi\sigma^{2n+4}\Gamma(n+2)}} \times (iA_1r^{|n|}e^{in\phi}, -A_2r^{|n+1|}e^{i(n+1)\phi}, iA_3r^{|n+2|}e^{i(n+2)\phi})^T, \quad (10)$$

where A_1, A_2, A_3 are the variational amplitudes, σ is the variational width of the *ansatz*, and n is a variational integer. In the absence of rotation, the ground state of the single particle Hamiltonian is a circularly symmetric $(-1, 0, +1)$ type multi-ring solution with ± 1 components hosting ∓ 1 phase-singularities [9]. This allows us to fix the integer $n \geq -1$. The normalization condition imposes the constraint

$$\left[\frac{A_1^2\Gamma(|n|+1)}{\sigma^{2(1-|n|+n)}\Gamma(n+2)} \right] + [A_3^2(n+2)\sigma^2 + A_2^2] = 1, \quad (11)$$

on the variational parameters A_1, A_2, A_3, n , and σ . The

variational energy in this case is

$$E_{\text{var}}(A_1, A_2, A_3, n, \sigma) = \frac{\sigma^{-2(n+2)}}{2\Gamma(n+2)} [(\sqrt{2}A_1A_2\gamma - |n|+3n+2)\sigma^{|n|+n+2}\Gamma\left(\frac{1}{2}(n+|n|+2)\right) + A_1^2\sigma^{2|n|}\Gamma(|n|+1) + ((\sigma^4+1)|n|-2n\sigma^2\Omega_{\text{rot}}+\sigma^4+1) + (n+1)\sigma^{2n+2}\Gamma(n+1) - (2\sqrt{2}A_2A_3\gamma(n+2)\sigma^2 + A_3^2(n+2)\sigma^2(n(\sigma^4-2\sigma^2\Omega_{\text{rot}}+1) + 3\sigma^4-4\sigma^2\Omega+3) + A_2^2(n\sigma^4-2n\sigma^2\Omega_{\text{rot}}+n+2\sigma^4-2\sigma^2\Omega_{\text{rot}}+2))]. \quad (12)$$

This energy can be minimized with respect to all variational parameters subject to the constraint in Eq. (11) to fix the variational parameters. To illustrate the validity of the variational method in this case, we consider three sets of parameters

$$\gamma = 0.5, \quad \Omega_{\text{coh}} = 0, \quad \Omega_{\text{rot}} = 0.95, \quad (13a)$$

$$\gamma = 1, \quad \Omega_{\text{coh}} = 0, \quad \Omega_{\text{rot}} = 0.5, \quad (13b)$$

$$\gamma = 1, \quad \Omega_{\text{coh}} = 0, \quad \Omega_{\text{rot}} = 0.95. \quad (13c)$$

The minimization of (12) results in $(A_1, A_2, A_3, n, \sigma) =$

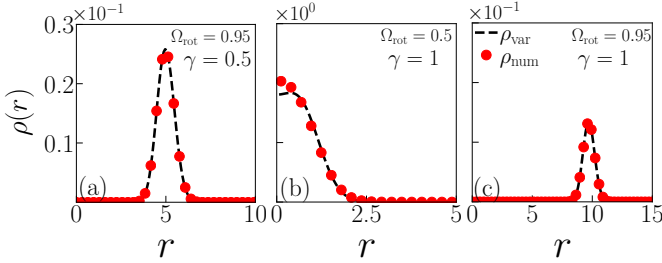


FIG. 2: (Color online) Total single-particle densities corresponding to variational (ρ_{var}) and exact numerical solution (ρ_{num}) of the eigen-value problem for (a) $\gamma = 0.5$, $\Omega_{\text{coh}} = 0$, $\Omega_{\text{rot}} = 0.95$; (b) $\gamma = 1$, $\Omega_{\text{coh}} = 0$, $\Omega_{\text{rot}} = 0.5$; and (c) $\gamma = 1$, $\Omega_{\text{coh}} = 0$, $\Omega_{\text{rot}} = 0.95$. The charges of phase singularities in the component wavefunctions corresponding to the total densities in (a), (b) and (c) are $(+25, +26, +27)$, $(0, +1, +2)$, and $(+98, +99, +100)$, respectively.

$(-2.512, 0.707, 0.097, 25, 0.975)$ for parameters' set (13a), $(A_1, A_2, A_3, n, \sigma) = (0.517, -0.675, -0.336, 0, 0.828)$ for (13b), and $(A_1, A_2, A_3, n, \sigma) = (-4.861, 0.707, 0.051, 98, 0.975)$ for (13c). The comparison of variational, $\rho_{\text{var}}(r) = |\Phi_{\text{var}}(r, \phi)^2|$, and exact numerically evaluated single-particle density profiles, $\rho_{\text{num}}(r)$, for (13a), (13b) and (13c) are shown in Figs. 2 (a), (b) and (c), respectively. The charges of phase singularities in the component wavefunctions obtained with the variational analysis, i.e., $(+25, +26, +27)$ for set (13a), $(0, +1, +2)$ for set (13b) and $(+98, +99, +100)$ for (13c) match with the exact numerical results. For the sets (13a), (13b), and (13c), the peaks of total variational densities lie along circles of radii 4.95, 0.67 and 9.74, respectively, and are reflective of the effective toroidal potential experienced by the boson.

III. ROTATING SO- AND COHERENTLY-COUPLED SPIN-1 BEC

In a typical experiment the BEC can have atom-number ranging from a few thousands to up-to a few tens of a million, which primarily interact via s -wave scattering. At temperatures very close to absolute zero, this ultra-dilute quantum degenerate system is usually studied using a mean-field approximation which neglects the quantum and thermal fluctuations. In the mean-field approximation, a rotating SO-coupled spin-1 BEC in a quasi-two-dimensional harmonic trapping potential $V(x, y)$ can be described by three coupled GPEs [8, 36], which in the dimensionless form are

$$i\frac{\partial\phi_{\pm 1}}{\partial t} = \mathcal{H}\phi_{\pm 1} + c_2(\rho_0 \pm \rho_-)\phi_{\pm 1} + c_2\phi_{\mp 1}^*\phi_0^2 - \frac{i}{\sqrt{2}}(\gamma_x\partial_x\phi_0 \mp i\gamma_y\partial_y\phi_0) + \frac{\Omega_{\text{coh}}}{\sqrt{2}}\phi_0, \quad (14a)$$

$$i\frac{\partial\phi_0}{\partial t} = \mathcal{H}\phi_0 + c_2\rho_+\phi_0 + 2c_2\phi_{+1}\phi_{-1}\phi_0^* - i\frac{\gamma_x}{\sqrt{2}} \times \partial_x(\phi_{+1} + \phi_{-1}) + \frac{\gamma_y}{\sqrt{2}}\partial_y(\phi_{+1} - \phi_{-1}) + \frac{\Omega_{\text{coh}}}{\sqrt{2}}(\phi_{+1} + \phi_{-1}), \quad (14b)$$

$$\mathcal{H} = \sum_{\nu=x,y} \frac{p_\nu^2}{2} + V(x, y) + c_0\rho - \Omega_{\text{rot}}L_z$$

$$\rho = \sum_{j=\pm 1,0} \rho_j, \quad \rho_j = |\phi_j|^2, \quad \rho_{\pm} = \rho_{+1} \pm \rho_{-1},$$

where c_0 and c_2 are interaction parameters. These are defined as

$$c_0 = \sqrt{8\pi\alpha} \frac{N(a_0 + 2a_2)}{3a_{\text{osc}}}, \quad c_2 = \sqrt{8\pi\alpha} \frac{N(a_2 - a_0)}{3a_{\text{osc}}}, \quad (15)$$

where α is the ratio of trapping frequency along axial direction to the radial x direction, N is the total number of atoms in the BEC, and a_0 and a_2 are the s -wave scattering lengths in total spin 0 and 2 channels, respectively. The coupled GPEs, viz. (14a)-(14b), can be numerically solved using, for instance, time-splitting methods [37–40].

A. Numerical solutions of coupled GPEs

We consider 10^5 atoms of spin-1 BECs like ^{87}Rb and ^{23}Na in an isotropic quasi-two-dimensional harmonic trap with $\alpha = 10$. The trapping frequencies are $\omega_x = \omega_y = 2\pi \times 10$ Hz resulting in $a_{\text{osc}}^{\text{Rb}} = 3.41 \mu\text{m}$ and $a_{\text{osc}}^{\text{Na}} = 6.63 \mu\text{m}$, respectively, for ^{87}Rb and ^{23}Na spinor BECs. The ferromagnetic ^{87}Rb has $a_0 = 101.8a_B$ and $a_2 = 101.4a_B$ [41], and anti-ferromagnetic ^{23}Na has $a_0 = 50a_B$ and $a_2 = 55.01a_B$ [42], where a_B is the Bohr radius. The resultant dimensionless interaction strengths for ^{87}Rb are $c_0 = 2482.21$ and $c_2 = -11.47$, and the same

for ^{23}Na are $c_0 = 674.91$ and $c_2 = 21.12$. We solve coupled GPEs (14a)-(14b) on a two-dimensional 512×512 spatial grid with a spatial-step size $\Delta x = \Delta y = 0.1$ and a temporal step size $\Delta t = 0.005$ using a time-splitting Fourier spectral method [37]. We calculate the stationary-state solutions by solving the coupled GPEs in imaginary time with an apt initial guess solution. In order to study the vortex-lattice states that can emerge as the minimum energy solutions of an SO-coupled spin-1 BEC in a rotating frame, we consider the following SO-coupling strengths

$$\gamma_x = 1, \gamma_y = 0; \quad \gamma = 0.5; \quad \gamma = 1, \quad (16)$$

where as defined earlier $\gamma = \gamma_x = \gamma_y$.

We first study the rotating SO-coupled ^{87}Rb and ^{23}Na spinor BECs with these SO-coupling strengths *without* coherent coupling. For which, we use the non-rotated ground states as the apt initial guess solutions to evolve the coupled GPEs (14a)-(14b) in imaginary time with $\Omega_{\text{rot}} \neq 0$. For $\gamma_x = 1, \gamma_y = 0$, the ground state is a plane-wave phase for ^{87}Rb and a stripe phase for ^{23}Na [8]. Here at small rotation frequencies, the phase-singularities (vortices) in the component wave functions exclusively align along the x -axis. The central-chain of holes in the individual component densities arising due to these phase-singularities with $\Omega_{\text{rot}} = 0.5$ is evident in Fig. 3(A) for ^{87}Rb and 3(C) for ^{23}Na . At still higher rotation frequency of $\Omega_{\text{rot}} = 0.95$, majority of vortices arrange themselves on both the sides of the central chain of vortices as shown in Figs. 3(B) and 3(D) for ^{87}Rb and ^{23}Na , respectively. The appearance of central chain of vortices, which appears along the line of the intersection of $V_{\text{eff}}^+(x, y)$ and $V_{\text{eff}}^-(x, y)$, is a generic feature of these systems with a sufficiently strong one-dimensional SO coupling [28, 29]. In both the systems, the symmetric effective double-well potential leads to the condensate occupying the pairs of potential minima at $(x = 0, y = \pm 0.67)$ and $(x = 0, y = \pm 9.74)$, respectively, when rotated with $\Omega_{\text{rot}} = 0.5$ and 0.95 . This can be seen more vividly in the coarse-grained total density defined as $\tilde{\rho}(\mathbf{r}) = \int C(\mathbf{r} - \mathbf{r}') \rho(\mathbf{r}') d\mathbf{r}'$, where $C(\mathbf{r} - \mathbf{r}')$ is a normalized Gaussian with a width larger than the average inter-vortex separation. The coarse-grained total density peaks at the minima of the effective potentials. To illustrate, we refer the reader to $\tilde{\rho}(\mathbf{r})$ in Figs. 4(A) and (B) corresponding to the total density in Figs. 3(A) and (B), respectively. The $\tilde{\rho}(\mathbf{r})$ peaks at $(x = 0, y = \pm 0.6)$ and $(x = 0, y = \pm 9.7)$, respectively, in the two cases. The role of effective potential on the ground-state solution, say $(\phi_{+1}, \phi_0, \phi_{-1})^T$, becomes obvious if one considers the unitary transformation $(\psi_{+1}, \psi_0, \psi_{-1})^T = U^\dagger(\phi_{+1}, \phi_0, \phi_{-1})^T$, where component wave-function ψ_j is subjected to an effective potential $V_{\text{eff}}^j(x, y)$ as discussed in Sec. II. The component densities obtained by transforming the solutions shown in Figs. 3(C) and (D) for ^{23}Na , for instance, are shown in Figs. 5(A) and (B), which as discussed in the Sec. II are the solutions corresponding to $\gamma_x S_z p_x$ coupling in

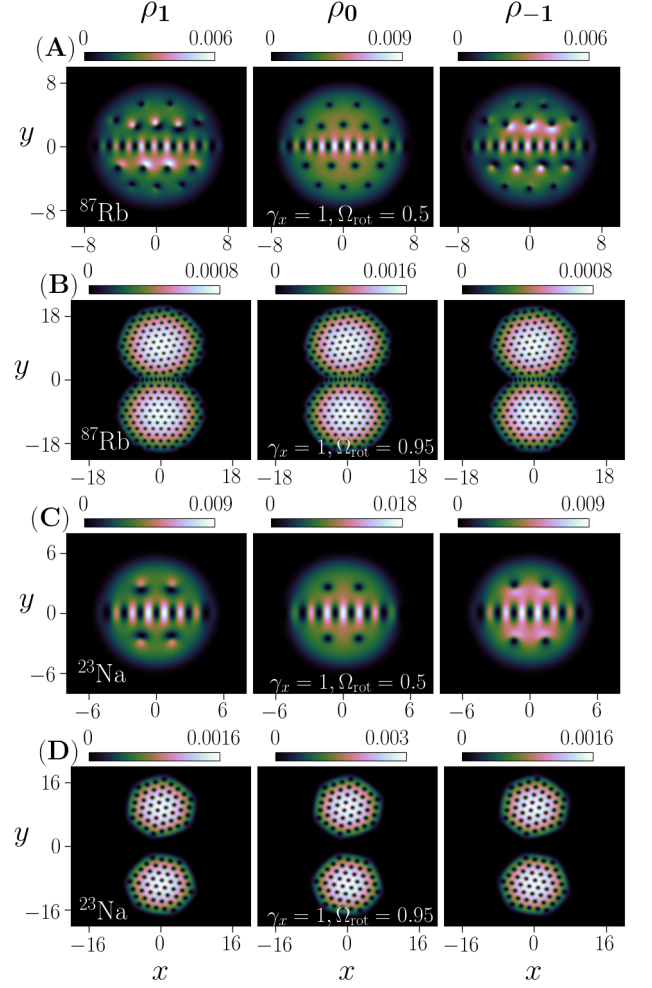


FIG. 3: (Color online) Equilibrium density profiles of the individual components of the SO-coupled ^{87}Rb spin-1 BEC with $c_0 = 2482.21$, $c_2 = -11.47$, $\gamma_x = 1$, and $\gamma_y = \Omega_{\text{coh}} = 0$: (A) with $\Omega_{\text{rot}} = 0.5$ and (B) with $\Omega_{\text{rot}} = 0.95$. Similarly, (C) and (D) show the component densities for ^{23}Na with $c_0 = 674.91$ and $c_2 = 21.12$. The spatial coordinates and densities are in the units of a_{osc} and a_{osc}^{-2} , respectively, where $a_{\text{osc}} = 3.41 \mu\text{m}$ for ^{87}Rb and $6.63 \mu\text{m}$ for ^{23}Na .

the mean-field model. The coarse-grained peak values of densities of $j = \pm 1$ components (which are not shown here) occur at $(0, \pm 0.6)$ and $(0, \pm 9.7)$ when rotated with $\Omega_{\text{rot}} = 0.5$ and 0.95 are in agreement with the effective potentials in Figs. 1(a) and (b), respectively. In the absence of rotation, $\gamma_x S_z p_x$ SO coupling favors miscibility of $j = \pm 1$ components for anti-ferromagnetic interactions, whereas it leads to phase-separation if the coupling strength is above a critical value for ferromagnetic interactions [43]. In the presence of rotation, the effective potential can lead to the phase-separation not only for a ferromagnetic ^{87}Rb (not shown here) but also for an antiferromagnetic ^{23}Na as is seen in the component density profiles in Figs. 5(A) and (B) for ^{23}Na . The $j = 0$

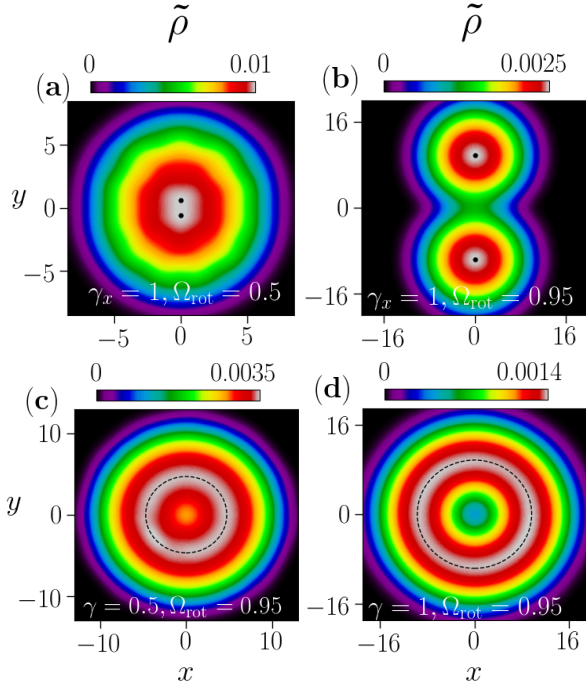


FIG. 4: (Color online) (a) and (b), respectively, show the coarse-grained densities $\tilde{\rho}(\mathbf{r})$ corresponding to the total densities in Figs. 3(A) and (B); the peak values of the coarse-grained densities at $(x = 0, y = \pm 0.6)$ and $(x = 0, y = \pm 9.7)$ are marked by dots. Similarly, (c) and (d), respectively, show $\tilde{\rho}(\mathbf{r})$ corresponding to the solutions in Figs. 6(B) and (D) and the respective peaks of $\tilde{\rho}(\mathbf{r})$ are marked by dashed circles of radii 4.7 and 9.7. The spatial coordinates and densities are in the units of a_{osc} and a_{osc}^{-2} , respectively, where $a_{\text{osc}} = 3.41 \mu\text{m}$.

component occupies the cores of vortices in $j = \pm 1$ component at $\Omega_{\text{rot}} = 0.5$ in Fig. 5(A). With an increase in rotation frequency, number of atoms in $j = \pm 1$ components keep on increasing at the cost of atoms in $j = 0$ component. Hence at larger rotation frequency of $\Omega_{\text{rot}} = 0.95$ in Fig. 5(B), there are no atoms in $j = 0$ component. Another consequence of the phase-separation is that the spin-expectation per particle (which is independent of rotation in spin space) tends to approach one for all the results shown in Fig. 5 and consequently in Fig. 3. Thus $\gamma_x S_z p_x$ SO coupling provides a simpler description of the results in Fig. 3.

Next for isotropic SO coupling with $\gamma = 0.5$ and $\Omega_{\text{rot}} = 0.5$, the small number of vortices which nucleate are unable to crystallize in a triangular vortex-lattice pattern as shown in Figs. 6(A) and 6(E) for ^{87}Rb and ^{23}Na , respectively, which are consistent with the observations in Refs. [30, 44]. The vortex patterns in the component densities near the center in Fig. 6(E) resemble square-lattices consistent with a similar observation in Ref. [30]. The two condensates rotated at a high rotation frequency $\Omega_{\text{rot}} = 0.95$ are shown in Figs. 6(B) and 6(F); here the phase profiles of both the condensates (which are not

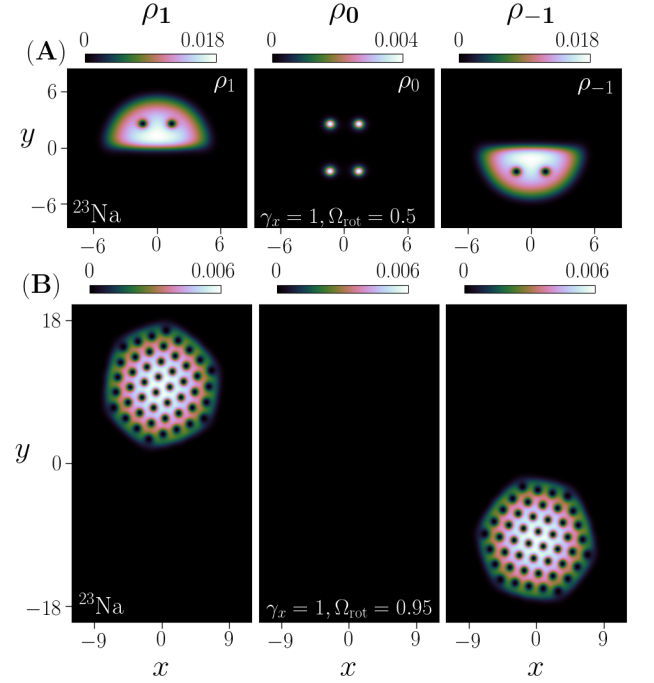


FIG. 5: (Color online) (A) and (B) are the individual component densities of the stationary SO-coupled spin-1 BECs of ^{23}Na corresponding to $H_{\text{SOC}} = \gamma_x p_x S_z$ for $\gamma_x = 1$ with $\Omega_{\text{rot}} = 0.5$ and $\Omega_{\text{rot}} = 0.95$, respectively. The $m_j = 0$ component is fully absent in (B). These solutions have been obtained by operating U^\dagger on the solutions corresponding to $H_{\text{SOC}} = \gamma_x p_x S_x$ shown in Figs. 3(C) and Figs. 3(D) for ^{23}Na BEC. The spatial coordinates and densities are in the units of a_{osc} and a_{osc}^{-2} , respectively, where $a_{\text{osc}} = 6.63 \mu\text{m}$ for ^{23}Na .

shown) reveals that the center of the condensates have phase singularities of charges $(0, +1, +2)$ in $j = +1, 0$, and -1 components, respectively. At this large rotation frequency more vortices are created in condensates which relax in a triangular lattice pattern. The coarse-grained peak value of the total densities for the two condensates lie along a circle of radius 4.7, e.g. $\tilde{\rho}(\mathbf{r})$ corresponding to the solution in Figs. 6(B) is shown in Fig. 4(C), which is in a decent agreement with the variational single-particle density maxima position in Fig. 2(a). The circle encloses approximately 26 phase singularities which agrees with phase-winding numbers calculated using variational analysis of the single-particle Hamiltonian. Next with $\gamma = 1$ and $\Omega_{\text{rot}} = 0.5$, the component ground-state densities are shown in Figs. 6(C) and 6(G). The centers of both the condensates in this case have phase singularities of charges $(0, +1, +2)$, respectively, in $j = +1, 0$, and -1 components, respectively. When rotated with higher frequency of $\Omega_{\text{rot}} = 0.95$, the condensate densities acquire a giant hole at the center as shown in Figs. 6(D) and 6(H) with an annulus of triangular vortex-lattice pattern in each component. The coarse-grained peak values of the total densities in this case too are along a circle of

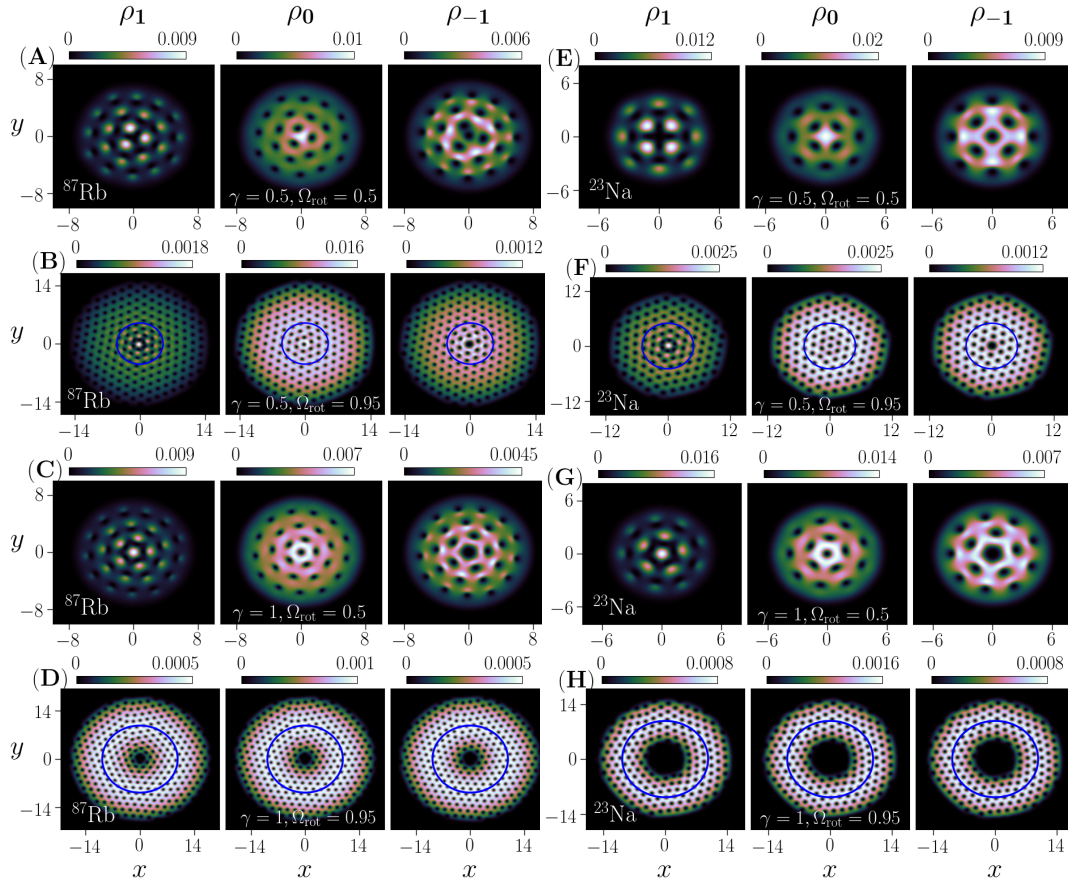


FIG. 6: (Color online) Equilibrium density profiles of the individual component densities of the SO-coupled spin-1 BECs: (A)-(D) ^{87}Rb with $c_0 = 2482.21$, $c_1 = -11.47$ and (E)-(H) ^{23}Na spin-1 BEC with $c_0 = 674.91$ and $c_2 = 21.12$. (A) and (B) have been obtained with $\Omega_{\text{rot}} = 0.5, 0.95$, respectively, and SO-coupling strength of $\gamma = 0.5$. Similarly, (C) and (D) correspond to SO-coupling strength of $\gamma = 1$ with $\Omega_{\text{rot}} = 0.5$, and 0.95 , respectively. For SO-coupled ^{23}Na , the plots (E) and (F) correspond to $\gamma = 0.5$ and $\Omega_{\text{rot}} = 0.5, 0.95$, respectively, and (G) and (H) correspond to $\gamma = 1$ with $\Omega_{\text{rot}} = 0.5, 0.95$, respectively. The spatial coordinates and densities are in the units of a_{osc} and a_{osc}^{-2} , respectively, where $a_{\text{osc}} = 3.41 \mu\text{m}$ and $6.63 \mu\text{m}$ for ^{87}Rb and ^{23}Na , respectively.

radius 9.7 as is seen in Fig. 4(D) for ^{87}Rb , which agrees well with the variational single-particle density peak in Fig. 2(c). The circle contains approximately 100 phase singularities in each component in agreement with the single particle. The appearance of a giant vortex at the trap center in the component densities surrounded by singly charged vortices arranged in an annulus for sufficiently strong isotropic SO-coupling strengths at fast rotations is a generic feature of these systems [20, 23]. The quantitative differences in respective component densities of ^{87}Rb and ^{23}Na when rotated with $\Omega_{\text{rot}} = 0.95$ is primarily a consequence of c_0 for the two BECs being 2482.21 and 674.91, respectively.

1. Effect of Coherent coupling

To highlight the effects which can solely be attributed to an interplay of rotation, coherent coupling, and inter-

actions, we first consider ^{23}Na BEC without and with coherent coupling at rotation frequency of $\Omega_{\text{rot}} = 0.95$ in the absence of SO coupling. Here without coherent coupling, the BEC supports an array of double-core vortices [50] in each component which arrange themselves in a square-lattice pattern as is shown in Figs. 7(A). Each double-core vortex core consists of two non-overlapping phase singularities of unit charge each which have been marked with white dots in Fig. 7(A). With coherent coupling of $\Omega_{\text{coh}} = 1$, the system at the same rotation frequency of $\Omega_{\text{rot}} = 0.95$ hosts a triangular-lattice pattern in each component as shown in Fig. 7(B), where a typical vortex core in each component consists of a single phase singularity. Here the effective potential is an isotropic harmonic potential V_{eff}^{-1} as shown in shown in Fig. 1(c).

Next we consider the combined effect of SO and coherent couplings on the ground-state vortex configurations. Here we consider two parameters sets- first with $\gamma_x = \gamma_y = 1$, $\Omega_{\text{coh}} = 1$, and second with $\gamma_x = 1$, $\gamma_y = 0$,

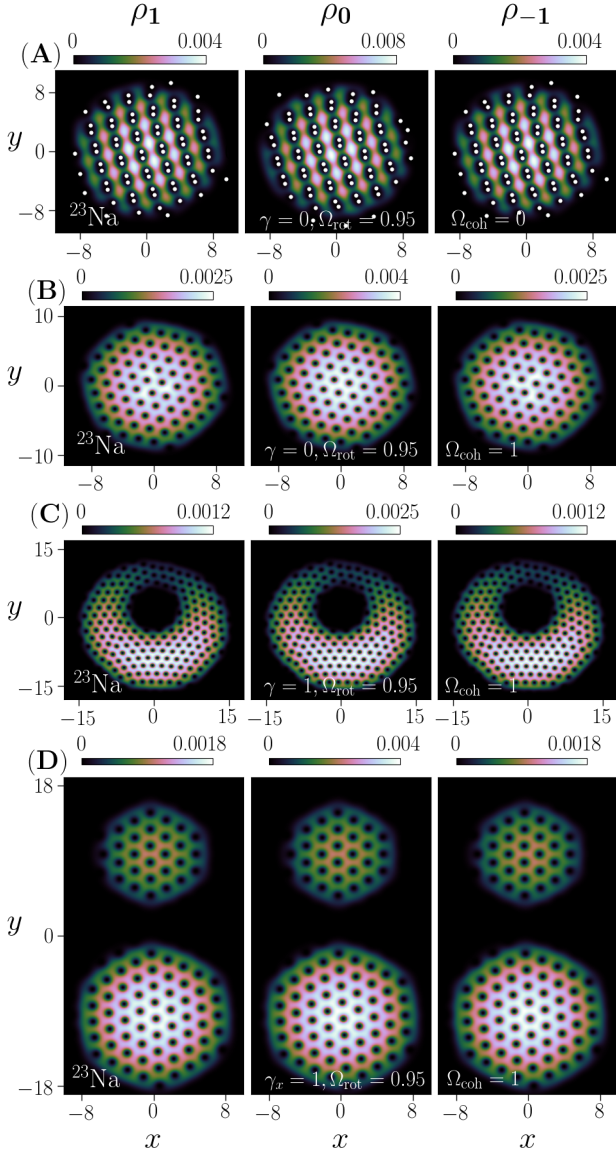


FIG. 7: (Color online) Equilibrium density profiles of the individual components of ^{23}Na spin-1 BEC with interaction parameters $c_0 = 674.91$, $c_2 = 21.12$, when rotated with $\Omega_{\text{rot}} = 0.95$. (A) has been obtained for $\Omega_{\text{coh}} = \gamma_x = \gamma_y = 0$ and $\Omega_{\text{rot}} = 0.95$, whereas (B), (C), and (D) have been obtained with coherent-coupling strength $\Omega_{\text{coh}} = 1$ and SO-coupling strengths of $\gamma_x = \gamma_y = 0$, $\gamma_x = \gamma_y = 1$, and $\gamma_x = 1, \gamma_y = 0$, respectively. The spatial coordinates and densities are in the units of $a_{\text{osc}}^{\text{Na}}$ and $[a_{\text{osc}}^{\text{Na}}]^{-2}$ respectively, where $a_{\text{osc}}^{\text{Na}} = 6.63 \mu\text{m}$.

$\Omega_{\text{coh}} = 1$. In the former case, the ground state density has a hole whose center is shifted along $+y$ direction as shown in Fig. 7(C). In the latter, the component densities distribute in two unequal triangular lattice patterns above and below x -axis as shown in Fig. 7(D), and with an increase in Ω_{coh} , the size of smaller triangular lattice pattern in the upper-half plane decreases further with a

corresponding increase in the size of one in the lower-half plane. The splitting of the component densities in two unequal parts can be attributed to the effective potential experienced by the system which is an asymmetric double-well potential created by $V_{\text{eff}}^{-1}(x, y)$ and $V_{\text{eff}}^{+1}(x, y)$ with a global minima at $(x = 0, y = -9.7)$ and a local minima at $(x = 0, y = +9.7)$ as shown in Fig. (1)(d). We obtain similar results for ^{87}Rb spin-1 BEC at $\Omega_{\text{rot}} = 0.95$ which have not been shown here.

B. Spin-expectation per particle and spin-texture

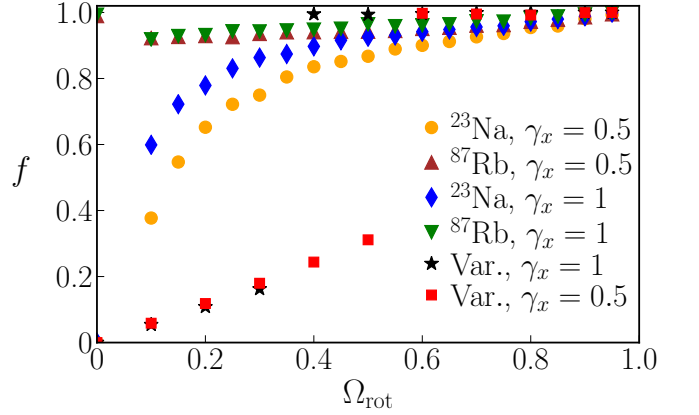


FIG. 8: (Color online) Variation of spin-expectation per particle f with rotation frequency obtained from the variational method discussed in Sec. II and the numerical solutions of the GPEs for the SO-coupled ^{87}Rb and ^{23}Na BECs.

As noted in Sec. III A, the ground state solutions of the rotating SO-coupled ^{87}Rb and ^{23}Na BECs at moderate to high rotation frequencies are qualitatively similar, and the quantitative differences stem from the different magnitudes of c_0 . To ascertain this further, here we consider SO-coupled ^{87}Rb and ^{23}Na spin-1 BECs with $\gamma = 0.5$ or 1 , $\Omega_{\text{coh}} = 0$ and (approximately) same c_0 but with different atom numbers. For ^{87}Rb , we again consider $c_0 = 2482.21$ and $c_2 = -11.47$ corresponding to 10^5 atoms, whereas for ^{23}Na we consider 3.68×10^5 atoms resulting in $c_0 = 2482.35$ and $c_2 = 77.68$. We define the spin-density vector $\mathbf{F} = (F_x, F_y, F_z)$ where

$$F_\nu(x, y) = \sum_{m, m'} \phi_m^*(x, y) (S_\nu)_{mm'} \phi_{m'}(x, y), \quad (17)$$

and $f = \int |\mathbf{F}(x, y)| d\mathbf{r} / \int \rho(x, y) d\mathbf{r}$, which serves as a measure of spin-expectation per particle for an inhomogeneous system. We examine the angular momentum per particle, f , and spin-texture [36] $\mathbf{f}(x, y) = \mathbf{F}(x, y) / \rho(x, y)$ as a function of rotation frequency. In the absence of rotation, the ^{87}Rb and ^{23}Na spin-1 BECs have $f = 1$ and 0 , respectively [36]. The f as a function of rotation frequency Ω_{rot} for the two systems is shown in Fig 8, which

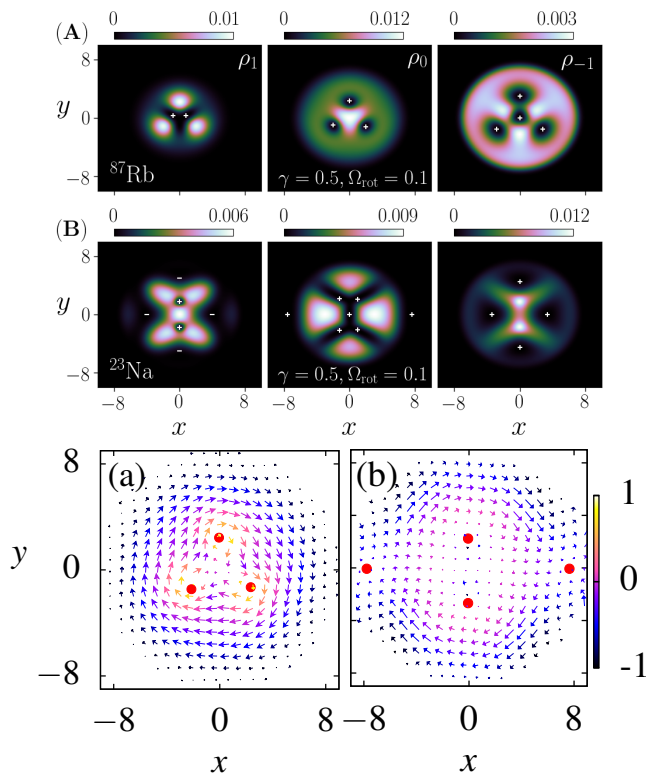


FIG. 9: (Color online) (A) displays the component density of the SO-coupled ^{87}Rb BEC with $\gamma_x = \gamma_y = 0.5$ when rotated with $\Omega_{\text{rot}} = 0.1$ and (B) displays the same for ^{23}Na BEC. The interaction strengths for ^{87}Rb and ^{23}Na are $c_0 = 2482.21$, $c_2 = -11.47$ and $c_0 = 2482.35$, $c_2 = 77.68$, respectively. The locations and signs of phase-singularities in each component are marked with \pm signs. (a) and (b), respectively, show the spin-textures corresponding to the densities in (A) and (B), where (a) has the three skyrmions (marked by red dots), and (b) has two near the center of the trap in addition to two cross-disgyrations in spin-texture along x -axis coinciding with $+1$ phase singularity in $m_f = 0$ component. The spatial coordinates and densities are in the units of a_{osc} and a_{osc}^{-2} , respectively, where $a_{\text{osc}} = 3.41 \mu\text{m}$ and $6.63 \mu\text{m}$ for ^{87}Rb and ^{23}Na , respectively.

illustrates that with increase in Ω_{rot} , $f \rightarrow 1$ for ^{23}Na whereas it remains close to 1 for ^{87}Rb . We also analyse spin-expectation per particle using the single-particle variational solution Φ_{var} in Eq.(10) to evaluate f . The variational analysis predicts $f \approx 1$ for $\gamma = 0.5$ (1) and $\Omega_{\text{rot}} \geq 0.6$ (0.4), which is consistent with the numerical results for ^{87}Rb and ^{23}Na BECs at moderate to high rotations as is shown in Fig. 8. The differences in numerical and variational f values for $\Omega_{\text{rot}} \leq 0.6$ (0.4) are mainly because of spin-dependent interactions, which expectedly become increasingly less important with an increase in rotation frequency. Next we consider the spin-texture of ^{87}Rb and ^{23}Na BEC with $\gamma = 0.5, \Omega_{\text{coh}} = 0$ when rotated with $\Omega_{\text{rot}} = 0.1$ and 0.95 . The component densities for ^{87}Rb and ^{23}Na when rotated with $\Omega_{\text{rot}} = 0.1$ are shown in Figs. 9(A) and (B), respectively, and the

corresponding spin textures are in Figs. 9(a) and (b). At this frequency ^{87}Rb hosts three skyrmions in Fig. 9(a) as compared to two for ^{23}Na in Fig. 9(b) (near the center of the trap). The generation of skyrmion and half-skyrmion excitations in rotating SO-coupled BECs is discussed in Refs. [22, 26]. The spin-textures at $\Omega_{\text{rot}} = 0.95$ are shown in Fig. 10(a) for ^{87}Rb and Fig. 10(b) for ^{23}Na , here both the systems have a skyrmion at the center surrounded by a lattice of half-skyrmions. The spin-texture of ^{87}Rb corresponds to the component densities shown in Fig. 6(B), whereas the component densities of ^{23}Na which are indistinguishable ^{87}Rb are not shown here. The similarity of the two systems at faster rotation is therefore also reflected in the spin-textures. The similarity in the re-

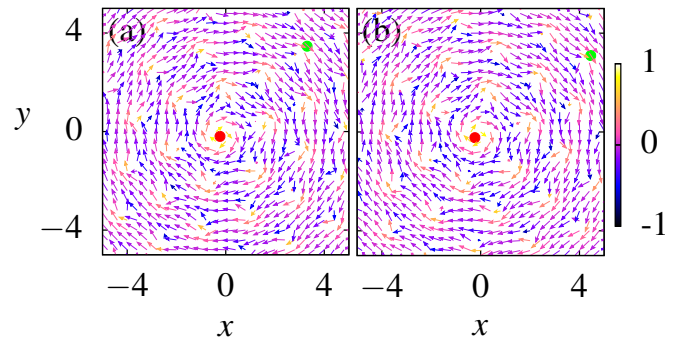


FIG. 10: (Color online) (a) shows the spin-texture for ^{87}Rb system and (b) shows the same for ^{23}Na system at rotation frequency $\Omega_{\text{rot}} = 0.95$. Both figures have a skyrmion at centre and in rest of the regions half skyrmions lattice. The respective interaction parameters are same as those considered in Fig. 9.

sponse of the two systems at fast rotations has also been confirmed based upon their mass and spin-currents.

IV. SUMMARY AND CONCLUSIONS

We have studied the effects of SO- and coherent-coupling on rotating ferro- and antiferromagnetic spin-1 BECs. Using exact numerical solutions complemented by a variational analysis, we have shown that the non-interacting part of the underlying spin-1 Hamiltonian can be translated to the rotating effective potentials with symmetric, asymmetric double-well, and toroidal structures. To this end, we have illustrated that using the mean-field Gross-Pitaevskii formalism, employing the realistic experimental parameters, the spatial distribution of ^{87}Rb and ^{23}Na BECs are consistent with the inhomogeneity of the effective potentials. The effects of rotation are further elucidated by computing the spin-expectation per particle for the ferro- as well as the antiferromagnetic BECs. For the former, the spin-expectation is always close to unity irrespective of the rotation frequency. While, for the latter, the spin-expectation value increases with an increase in rotation frequency and tends to ap-

proach one. For the simpler one-dimensional coupling ($\propto \gamma S_z p_x$), spatial segregation between the $j = \pm 1$ components results in spin-expectation per particle approaching one for the antiferromagnetic BEC; similarly, single-particle variational analysis with Rashba SO coupling also indicates the spin-expectation per particle approaching one irrespective of the spin-exchange interactions with increasing rotational frequency. The similarity in response of the fast-rotating ferromagnetic ^{87}Rb and antiferromagnetic ^{23}Na highlights the much diminished role of the spin-exchange interactions vis-à-vis the other competing terms in the system's Hamiltonian.

Acknowledgements

AR acknowledges the support of Science & Engineering Research Board (SERB), Department of Science

and Technology, Government of India under the project SRG/2022/000057 and IIT Mandi seed-grant funds under the project IITM/SG/AR/87. RKK is supported by the Marsden Fund of New Zealand (Contract No. UOO1726). SG acknowledges support from the Science and Engineering Research Board, Department of Science and Technology, Government of India through Projects No. ECR/2017/001436 and No. CRG/2021/002597.

-
- [1] Y.-J. Lin, R. L. Compton, K. Jimenez-García, J. V. Porto, and I. B. Spielman *Nature* **462**, 628 (2009).
 - [2] Y.-J. Lin, R. L. Compton, K. Jiménez-García, W. D. Phillips, J. V. Porto, and I. B. Spielman, *Nature Physics* **7**, 531 (2011).
 - [3] Y.-J. Lin, K. Jimenez-García, and I. B. Spielman, *Nature* **83**, 471 (2011).
 - [4] I. E. Rashba and Y. A. Bychkov *Journal of Physics C* **17**, 6039 (1984).
 - [5] G. Dresselhaus, *Phys. Rev.* **100**, 580 (1955).
 - [6] D. L. Campbell, R. M. Price, A. Putra, A. Valdés-Curiel, D. Trypogeorgos, and I. B. Spielman, *Nat. Commun.* **7**, 10897 (2016).
 - [7] Z. Wu, L. Zhang, W. Sun, X.-T. Xu, B.-Z. Wang, S.-C. Ji, Y. Deng, S. Chen, X.-J. Liu, and J.-W. Pan, *Science* **354**, 83 (2016).
 - [8] C. Wang, C. Gao, C. M. Jian, and H. Zhai, *Phys. Rev. Lett.* **105**, 160403 (2010).
 - [9] E. Ruokokoski, J. Huhtamäki, and M. Möttönen, *Phys. Rev. A* **86**, 051607(R) (2012).
 - [10] G. I. Martone, F. V. Pepe, P. Facchi, S. Pascazio, and S. Stringari, *Phys. Rev. Lett.* **117**, 125301 (2016).
 - [11] H. Zhai, *Int. J. of Mod. Phys.B*, **26** 1230001 (2012); H. Zhai, *Physics Reports* **78**, 026001 (2015).
 - [12] S. Gautam and S. K. Adhikari, *Phys. Rev. A* **95**, 013608 (2017).
 - [13] S. Gautam and S. K. Adhikari, *Phys. Rev. A* **97**, 013629 (2018); S. Gautam and S. K. Adhikari *Braz. J. Phys.* **51**, 298 (2021).
 - [14] Y.-K. Liu, Y. Liu, and S.-J. Yang, *Phys. Rev. A* **99**, 063626 (2019).
 - [15] S. K. Adhikari, *Phys. Rev. A* **103**, L011301 (2021).
 - [16] H.-R. Chen, K.-Y. Lin, P.-K. Chen, N.-C. Chiu, J.-B. Wang, C.-A. Chen, P. Huang, S.-K. Yip, Y. Kawaguchi, and Y.-J. Lin, *Phys. Rev. Lett.* **121**, 113204 (2018).
 - [17] P.-K. Chen, L.-R. Liu, M.-J. Tsai, N.-C. Chiu, Y. Kawaguchi, S.-K. Yip, M.-S. Chang, and Y.-J. Lin, *Phys. Rev. Lett.* **121**, 250401 (2018).
 - [18] J. Dalibard, F. Gerbier, G. Juzeliūnas, and P. Öhberg, *Rev. Mod. Phys.* **83**, 1523 (2011); N. Goldman, G. Juzeliūnas, P. Öhberg, and I. B. Spielman, *Rep. Prog. Phys.* **77**, 126401 (2014).
 - [19] J. Radić, T. A. Sedrakyan, I. B. Spielman, and V. Galitski, *Phys. Rev. A* **84**, 063604 (2011); J. Radić, *Spin-orbit-coupled quantum gases* (2015) [Doctoral dissertation, Maryland University].
 - [20] X.-Q. Xu and J. H. Han, *Phys. Rev. Lett.* **107**, 200401 (2011).
 - [21] X.-F. Zhou, J. Zhou, and C. Wu, *Phys. Rev. A* **84**, 063624 (2011).
 - [22] C.-F. Liu, H. Fan, Y.-C. Zhang, D.-S. Wang, and W.-M. Liu, *Phys. Rev. A* **86**, 053616 (2012).
 - [23] A. Aftalion and P. Mason, *Phys. Rev. A* **88**, 023610 (2013).
 - [24] H. Wang, L. Wen, H. Yang, C. Shi, and J. Li, *J. Phys. B: At. Mol. Opt. Phys.* **50**, 155301 (2017). C. Shi, L. Wen, Q. Wang, H. Yang, and H. Wang, *J. Phys. Soc. Jpn.* **87**, 094003 (2018); H. Yang, Q. Wang, N. Su, and L. Wen, *Eur. Phys. J. Plus*, **134**, 589 (2019); Q.-B. Wang, H. Yang, N. Su, and L.-H. Wen, *Chin. Phys. B* **29**, 116701 (2020); J.-G. Wang and Y.-Q. Li, *Results in Physics* **17**, 103099 (2020).
 - [25] A. Aftalion and P. Mason, *Phys. Rev. A* **94**, 023616 (2016).
 - [26] C.-F. Liu and W. M. Liu, *Phys. Rev. A* **86**, 033602 (2012);
 - [27] S.-W. Su, C.-H. Hsueh, I.-K. Liu, T.-L. Horng, Y.-C. Tsai, S.-C. Gou, and W. M. Liu, *Phys. Rev. A* **84**, 023601 (2011).
 - [28] C.-F. Liu, Y.-M. Yu, S.-C. Gou, and W.-M. Liu, *Phys. Rev. A* **87**, 063630 (2013).
 - [29] Q. Zhao and H. Bi, *Int. J. Theor. Phys.* **60**, 2778 (2021).
 - [30] S. K. Adhikari, *J. Phys.: Condens. Matter* **33**, 065404 (2021).
 - [31] P. Peng, G.-Q. Li, W.-L. Yang, and Z.-Y. Yanga, *Phys. Lett. A* **382**, 2493 (2018); X.-F. Zhang, B. Li, and S.-G. Zhang, *Laser Phys.* **23**, 105501 (2013).
 - [32] J. Li, X.-F. Zhang, and W.-M. Liu, *Ann. Phys.* **87** 396 (2018).
 - [33] G.-P. Chen, P. Tu, C.-B. Qiao, J.-X. Zhu, Q. Jia, and

- X.-F. Zhang, *Frontiers in Physics*, **9**, 613 (2021).
- [34] H. Zhu, C.-F. Liu, D.-S. Wang, S.-G. Yin, L. Zhuang, and W.-M. Liu, *Phys. Rev. A* **104**, 053325 (2021).
- [35] C.-T. Claude, D. Bernard, and L. Franck, *Quantum mechanics*, (New York, Wiley, 1977); R. Shankar, *Principles of Quantum Mechanics*, (Yale University, New Haven Connecticut Springer, 1994).
- [36] Y. Kawaguchi and M. Ueda, *Physics Reports* **520**, 253 (2012).
- [37] P. Kaur, A. Roy, and S. Gautam, *Comp. Phys. Comm.* **259**, 107671 (2021).
- [38] P. Banger, P. Kaur, S. Gautam, *Int. J. Mod. Phys. C* **33(4)**, 2250046 (2022).
- [39] R. Ravisankar, D. Vudragović, P. Muruganandam, A. Balaž, and S. K. Adhikari, *Comp. Phys. Comm.* **259**, 107657 (2021); P. Muruganandam, A. Balaž, and S. K. Adhikari, *Comp. Phys. Comm.* **264**, 107926 (2021).
- [40] P. Banger, P. Kaur, A. Roy, and S. Gautam, *Comp. Phys. Comm.* **279**, 108442 (2022).
- [41] E. G. M. V. Kempen, S. J. J. M. F. Kokkelmans, D. J. Heinzen, and B. J. Verhaar, *Phys. Rev. Lett.* **88**, 093201 (2002).
- [42] A. Crubellier, O. Dulieu, F. M. Seeuws, M. Elbs, H. Knöckel, and E. Tiemann, *Eur. Phys. J. D* **6**, 211 (1999).
- [43] S. Gautam and S. K. Adhikari, *Phys. Rev. A* **90**, 043619 (2014).
- [44] J. R. Abo-Shaeer, C. Raman, J. M. Vogels, and W. Ketterle, *Science*, **292**, 476479 (2001).
- [45] P. Kaur, S. Gautam, and S. K. Adhikari, *Phys. Rev. A* **105**, 023303 (2022).
- [46] S. Choi, S. A. Morgan, and K. Burnett, *Phys. Rev. A* **57**, 4057 (1998).
- [47] M. Tsubota, K. Kasamatsu, and M. Ueda, *Phys. Rev. A*, **65**, 023603 (2002).
- [48] M.-O. Mewes, M. R. Andrews, N. J. van Druten, D. M. Kurn, D. S. Durfee, C. G. Townsend, and W. Ketterle, *Phys. Rev. Lett.* **77**, 988 (1996); D. S. Jin, M. R. Matthews, J. R. Ensher, C. E. Wieman, and E. A. Cornell, *Phys. Rev. Lett.* **78**, 764 (1997).
- [49] K. Kasamatsu, M. Tsubota, and M. Ueda, *Phys. Rev. A* **67**, 033610 (2003); T. Mithun, K. Porsezian, and B. Dey, *Phys. Rev. A* **89**, 053625 (2014); T. Mithun, K. Porsezian, and B. Dey, *Phys. Rev. A* **93**, 013620 (2016); T. Mithun, S. C. Ganguli, P. Raychaudhuri, and B. Dey, *Europhysics Letters* **123**, 20004 (2018).
- [50] K. Kasamatsu, M. Tsubota, and M. Ueda, *International Journal of Modern Physics B* **19**, 1835 (2005).
- [51] S. Gautam and S. K. Adhikari, *Laser Phys. Lett.* **12**, 045501 (2015).